UNIVERSITY OF ZIELONA GÓRA

CEER CIVIL AND ENVIRONMENTAL ENGINEERING REPORTS

CIVIL AND ENVIRONMENTAL ENGINEERING REPORTS

E-ISSN 2450-8594

CEER 2025; 35 (3): 0108-0135
DOI: 10.59440/ceer-205775
Original Research Article

THE USE OF MULTISENSOR DRONE MONITORING TO FAULT'S ZONES IN AREAS AFFECTED BY MINING ACTIVITIES

Marcin PAWLIK [1], Quynh Anh NGUY, Bodo BERNSDORF, Tobias RUDOLPH, Benjamin HASKE
Research Center of Post-Mining, Technische Hochschule Georg Agricola, Bochum, Germany

A b s t r a c t

This study explores the use of advanced drone technology with multiple sensors to improve the detection and mapping of fault zones. The goal is to validate a multifaceted approach using LIDAR, multispectral cameras, and thermal imaging, providing a comprehensive analysis of the Earth's surface. LIDAR technology plays a critical role by creating high-resolution digital elevation models (DEMs) and digital surface models (DSMs). These models offer detailed depictions of terrain topography, crucial for identifying subtle variations associated with fault lines. LIDAR's ability to see through vegetation also aids in delivering a clear terrain representation, irrespective of surface cover. Multispectral cameras capture images across various wavelengths, enabling the analysis of vegetation health through indices like GNDVI, NDVI, MSAVI, and VARI. These indices indicate geological disruptions, such as fault zones, since vegetation health often correlates with underlying anomalies. Thermal imaging adds another dimension by detecting minor temperature fluctuations on the ground's surface. These variations can signal active faults, revealing friction or geothermal activities beneath the surface. To verify the sensor data accuracy, a site visit was conducted, comparing drone findings with actual soil profile samples. This ground-truthing step is vital for confirming that remote sensing data reflects real-world conditions accurately. Overall, the study shows that a multisensorial approach using drones significantly enhances fault zone detection and analysis. This integrated method serves as a potent tool for geological research, aiding in understanding fault dynamics and contributing to natural disaster preparedness.

Keywords: geomatics, multisensory UAV, geomonitoring, fault zone, mining activity

1. INTRODUCTION

Recent advancements in Unmanned Aerial Vehicles (UAVs) have immensely impacted the mining industry, providing innovative research possibilities and powerful analytical tools. As described by Shahmoradi [1], drones equipped with advanced sensors play a pivotal role in monitoring mine conditions, enhancing risk management, and optimizing operations. They offer high-resolution data

[1] Corresponding author: Marcin P. Pawlik, Technische Hochschule Georg Agricola, Research Center of Post-Mining, Herner Straße 45, 44787 Bochum, Germany, e-mail: Marcin.Pawlik@thga.de , telephone: +49 234 968-3805

crucial for accurate terrain mapping and hazard identification, which leads to improved resource management efficiency.

The influence of mining activities, particularly near tectonic fault zones, on the surrounding environment is considerable. Such operations can result in landslides, subsidence, and damage to infrastructure like roads and buildings [2,3]. The European Union Directive 2011/92 [4] emphasizes the need for comprehensive environmental impact assessments to address these effects. In our study, we focus on whether UAV technology can effectively monitor the Viersen fault zone near the Garzweiler II mine in western Germany, a zone potentially activated by mining activities.

Johansen et al. [5] present the rehabilitation of open-cut coal mines further illustrates how drones assess environmental recovery, tracking changes and assessing vegetation health to ensure effective reclamation efforts. Moreover, the Kim et al. [6] underscores the utility of drones for monitoring mine structures through 3D imaging, predicting future changes essential for sustainable mining practices.

Together, these insights demonstrate the versatility of drone technology, enabling a comprehensive and integrated approach to managing environmental and operational challenges in mining. By transforming traditional methods of supervision and analysis, drones provide a precise and dynamic framework essential for addressing the complexities of mining activities and ensuring long-term geological stability and sustainability.

Table 1. Brief overview over UAV application in land and water monitoring incl. references

UAV Application	Publication | Reference
environmental monitoring (multispectral)	[7-10]
monitor water acidity and effects of mining activities (hyperspectral)	[11-14]
detection of disaster-affected areas (thermal)	[15-17]
monitoring of post-mining waste heaps	[18,19, 140]
inspection of the oil, gas, and mining industries	[20-24]
surface scanning enables / digital terrain models and orthophotos (laser)	[25, 140]
landslides	[27-39]
stream reclamation	[26]
identification of geological structural elements	[40,41]
slope stability observations	[42,43]
fault identification	[38, 44-47]

In this study, we utilized drone flights equipped with multispectral, thermal cameras, and laser scanners. Our The goal was to use unmanned aerial vehicles to monitor the possibly mining induced activatede Viersen fault zone located near the Garzweiler II mine in western Germany, as its observation is very important to prevent possible consequences. To date, fault identification in the literature has been based on calculated digital terrain models. However, in this study, we used multisensory monitoring (multispectral data, thermal data, and point clouds) to reconstruct the fault's location. The integration and fusion of the obtained data allow for the visualization of the fault's location and its impact on the surrounding environment. Using multisensory monitoring, it is possible to reconstruct the fault's location, which will enable the future application of this method for mapping active faults and assessing seismic hazards for areas near open-pit coal mines – thus, the base for a geomonitoring concept.

2. STUDY AREA

The study area is located in the western part of Germany, near the district of Mönchengladbach – Sasserath (Fig. 1), and to the north of the Garzweiler II open-pit coal mine.

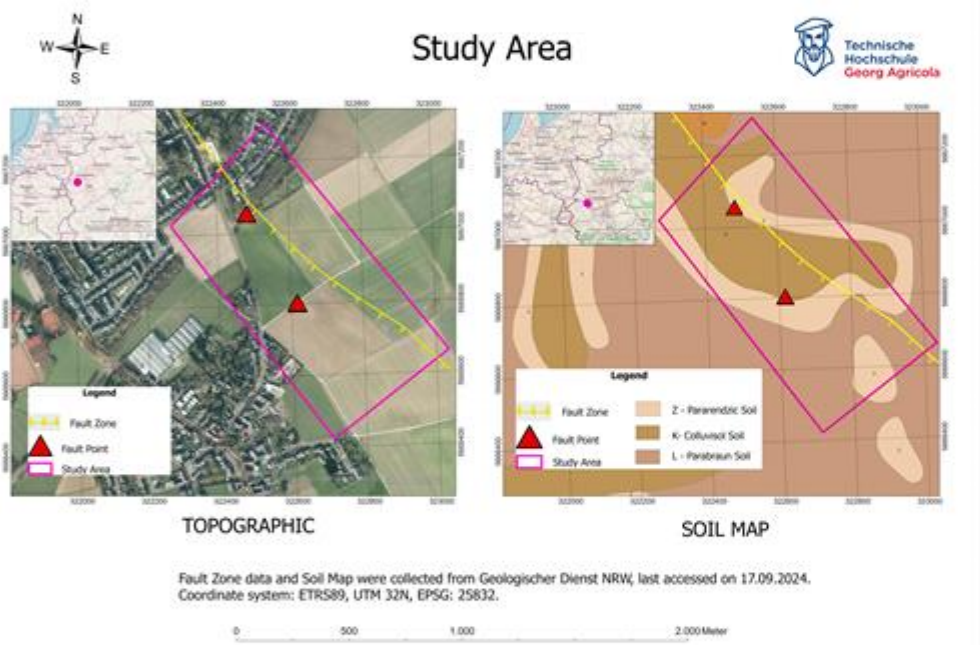

Fig. 1. Localization of study area. Source of basemaps: ESRI (left), Soil Map of NRW 1:50000 – Geological Survey of North-Rhein Westphalia, Data License – Germany – attribution - version 2.0 (right) [48]

2.1. Geological Research

Mönchengladbach-Sasserath is an area with a complex geological and tectonic structure, located within the Lower Rhine Valley, which is part of a larger tectonic structure known as the Lower Rhine Rift. This area is characterized by a series of sedimentary basins formed as a result of tectonic subsidence during the Tertiary period [49]. The main tectonic structures of this area are associated with normal faults oriented NW-SE [49,50,55], including the Rur, Erft, Swiss, Jackerather Horst, and Viersen faults. These faults are responsible for the formation of deep sedimentary basins filled with marine, fluvial, and deltaic sediments. As noted by Klostermann [49], the boundary between the western and eastern parts of the Lower Rhine Bay (German: Niederrheinische Bucht) runs along the western edge of the Viersen fault.

The Tertiary sediments, which dominate the subsurface of Mönchengladbach-Sasserath, consist of the Cologne Formation, the Inden Formation, and the Hauptkies Formation, which contain lignite seams as well as numerous clastic interbeds of fluvial and marine origin [51,53,54]. The most important lignite seams in this area are Morken, Frimmersdorf, and Garzweiler [53,58], which reach a thickness of up to 100 meters [52,57,59]. In the later stages of sedimentation during the Pliocene, the fluvial sediments of the Rotton and Reuver formations covered the older units, creating a complex stratigraphic record of the tectonic and sedimentary development of this region [57].

As a result of ongoing tectonic activity and erosion processes, these structures have been partially deformed, affecting the complex geometry of the coal seams and other stratigraphic features of this region [51,56]. Despite these complexities, accurate stratigraphic correlation is possible thanks to numerous geological studies, including the analysis of drilling logs conducted in this area [51].

2.2. Seismical Research

The literature, particularly the works of Ahorner [60,61], emphasizes the historical seismicity and contemporary tectonic activity in the Rhenish Massif, which affects the Mönchengladbach-Sasserath research area. Ahorner [61] points out that the pattern of seismotectonic displacements in Central Europe, including the Lower Rhine Valley, is the result of complex tectonic interactions that can lead to significant earthquakes, such as the one that occurred in Liège in 1983. The most recent earthquake with a magnitude of 5.9 occurred on April 18, 1992, near the city of Roermond (Netherlands) [55,56]. Camelbeeck et al. [55] provide a detailed analysis of the significance of studies on active faults and seismicity in the context of assessing long-term seismic activity (1382-1992) and the maximum possible earthquake magnitude in north-western Europe (Fig.2), including the Sasserath region. The authors note that the Lower Rhine Rift, where Sasserath is located, is one of the most tectonically active intraplate areas in Europe. Faults such as the Rurrand and Viersen, which run through this region, can be sources of significant tectonic movements and associated seismic activity [56,62,63].

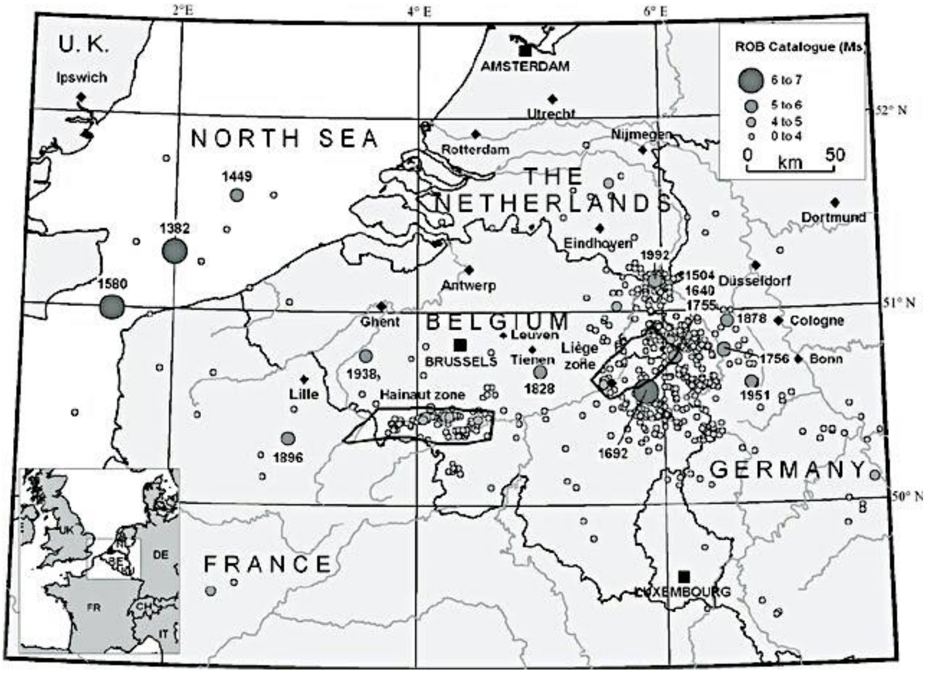

Fig. 2. Seismicity between the Lower Rhine Embayment and the southern North Sea [55]

Gold et al. [64] and Grützner et al. [65] also provide evidence of increased fault activity in the late Quaternary, which may indicate a heightened seismic risk in the future. Specifically, Grützner et al. [65] document surface ruptures associated with the Rurrand fault, suggesting that these faults remain active and could lead to significant seismic events. Reicherter et al. [56] add that the influence of Alpine tectonics north of the Alps, including in the Lower Rhine Valley, contributes to the complex tectonic dynamics in the region, potentially increasing seismic risk and affecting the development of tectonic structures in the Sasserath area. Geophysical studies and seismic modelling have shown that there are significant differences in sediment thickness in the region, which affects the propagation of seismic waves and may increase the risk of local earthquakes [66,67]. Additionally, the continuous withdrawal of groundwater and mining activities in the lignite mining area can also impact land stability and induce seismic activity around the Erft fault [68]. Furthermore, Petri's [69] research highlights the impact of mining activities, particularly in the context of lignite extraction in the Rhenish Mining District, on slope stability and induced seismic activity. The exploitation of resources in this region, combined with natural tectonic activity, may lead to further surface deformations and an increase in seismic hazards. In conclusion, the Mönchengladbach-Sasserath area is a region with a high tectonic risk, with active faults that are continuously monitored due to their potential to generate significant seismic events. Geological and seismological studies suggest that this region will remain susceptible to seismic activity in the future, necessitating further research and risk management measures.

2.3. Mining Activity in Garzweiler II

Garzweiler II is one of the largest open-pit lignite mines in Germany (Fig. 3), situated in the Rhenish Mining District in North Rhine-Westphalia and operated by RWE Power AG. The mine, covering an area of approximately 48 square kilometers, has been a key source of lignite since mining activities began in the 1980s, with full-scale operations commencing in the 1990s. Annually, Garzweiler II produces around 35 million tons of lignite, which is primarily used to fuel nearby power plants, providing a significant portion of Germany's electricity supply.

The mining operations have had substantial environmental and social impacts, particularly through the resettlement of thousands of residents from villages within the mining area. This process has involved extensive landscape alterations, including the removal of high potential topsoil (brown, para brown and black soils on Loess) and the relocation of infrastructure such as roads and railways. RWE has been actively involved in these resettlement efforts and has undertaken land reclamation projects aimed at restoring the mined land for future uses, including agricultural and recreational purposes.

Garzweiler II has also been at the center of environmental debates, particularly in the context of Germany's energy transition and the country's goals to reduce carbon emissions. While the mine is crucial for meeting current energy demands, it presents challenges in balancing these needs with environmental sustainability. RWE has faced criticism from environmental groups and local communities regarding the long-term environmental impact of lignite mining, especially its contribution to CO2 emissions. In response, RWE has committed to phasing out lignite by 2038, in line with Germany's coal exit plan.

Fig. 3. Garzweiler open-pit lignite mines

3. METHODOLOGY

The methodology of drone flights involves a series of steps and procedures aimed at ensuring safety, regulatory compliance, and achieving the desired outcomes from the flight. First, the flight must be carefully planned, considering the mission's objective as well as the local topography, airspace obstacles, and weather conditions, including wind speed, maximum gusts, precipitation, and air temperature. Next, it is essential to check whether the area in question is subject to restricted access and obtain any necessary permits (such as residential areas, airports, industrial or military zones) in accordance with local drone flight regulations. In Germany, the legal basis at the national level (LuftVG (Luftverkehrsgesetz) [70], LuftVO (Luftverkehrs-Ordnung) [71], LuftVZO (Luftverkehrs-Zulassungs-Ordnung[72])) has been adapted by the "Act to adapt national regulations to Commission Implementing Regulation (EU) 2019/947 of 24 May 2019 on the rules and procedures for the operation of unmanned aircraft" [73]. According to the law all drone pilots of FZN owns a license covering A1, A2 and A3 level.

The next step is a risk analysis, which involves identifying potential hazards and risks associated with the flight and developing contingency plans. After the planning stage, the drone must be prepared for flight. This process involves conducting a pre-flight inspection, which includes checking the drone's technical condition, including the batteries, engines, navigation systems, and communication. It is also important to ensure that the software and maps are up-to-date and that all settings are configured for the planned flight. The next stage is the execution of the flight, during which flight parameters such as battery level, GNSS signal quality, altitude, and flight speed must be monitored. In case of any issues, it is important to be prepared to implement previously developed emergency procedures. In all flights there are in minimum two pilots involved. One as the drone controller the other as airspace observer – both with equal qualification.

After the flight, the collected data is analyzed and processed. Depending on the mission's objective, this may involve image processing, 3D models creation, measurement analysis, or the preparation of an inspection report. It is also advisable to review the entire flight process to identify areas for improvement and optimize future missions. Such a systematic methodology ensures safe and effective drone flights and the achievement of intended goals.

3.1. LiDAR

LiDAR technology (Light Detection and Ranging) used as a sensor during drone flights is increasingly gaining popularity due to its ability to precisely map terrain, especially in hard-to-reach and vast areas [74]. This technology enables the collection of 3D topographical data of landscapes [74] and the study of vegetation, including its density, surface area, and structure [74-77].

Thanks to point clouds obtained by the laser scanner, it is possible to create a grid of triangles/squares to generate a Digital Surface Model (DSM) and a Digital Elevation Model (DEM). Bater and Coops [78]. present in their article an assessment of errors associated with the interpolation of digital terrain models derived from LiDAR data. This study allows understanding how different interpolation methods (Kriging, nearest neighbor method, or inverse distance weighting – IDW) can affect the quality and accuracy of the generated models. Hancock [79] also conducted studies on the impact of different mesh modeling techniques on the resulting terrain model. In generating digital terrain models, it is particularly important to consider the variability of spatial data, so the choice of interpolation method should be based on the specifics of the terrain and the purpose of the analysis.

As indicated by Lin et al. [74], although the spatial resolution of terrestrial LiDAR data is significantly higher than that of aerial data, the point density significantly decreases as the scanner's distance from the object increases. To obtain a dense point cloud across the entire area of interest, it is often necessary to position multiple ground-based LiDAR scanning stations. A registration process is required to integrate individual scans into a single mapping framework, which involves measuring several ground control points (GCP) or manually selecting common points from overlapping point clouds. Due to the prolonged duration of fieldwork and data processing, terrestrial LiDAR scanning is usually limited to selected areas of interest, as larger-scale analyses are impractical.

Compared to terrestrial LiDAR, research using UAVs offers significant advantages, such as lower equipment costs, faster execution times, ease of deployment, and fewer limitations in fieldwork [80, 81]. The resolution and accuracy of SfM methods are generally comparable to terrestrial LiDAR, and both technologies show good agreement with GNSS data [81,82]. However, UAV photogrammetry is more susceptible to environmental conditions, as 3D reconstruction from images is more difficult in low-texture areas. Studies also show a lack of quality assessment of UAV photogrammetry in various geomorphological environments [80,82,83]. Thanks to recent advances in UAV and LiDAR technologies and reduced integration costs, UAV LiDAR is gaining popularity in fields such as forestry, archaeology, and infrastructure monitoring [74, 83-89].

In this research we used the DJI Zenmuse L1 (Fig. 4), who is an advanced LIDAR sensor developed by DJI, designed for use with drones such as the DJI Matrice 300 RTK. This device is equipped with a Livox LIDAR module, capable of emitting up to 240,000 points per second, allowing for rapid and precise 3D data collection. The Zenmuse L1 is characterized by its high accuracy, offering vertical accuracy within 5 cm and horizontal accuracy within 10 cm when using RTK, making it an extremely precise tool for mapping and engineering applications. Additionally, the sensor features a 20 MP RGB camera with a mechanical shutter, enabling the capture of high-resolution images that can be integrated with LIDAR data, facilitating the creation of photorealistic 3D models. The Zenmuse L1 offers multi-directional scanning with a 70° horizontal and 4° vertical field of view, allowing data to be collected over a wide area in a single pass. The sensor also includes a built-in IMU (Inertial Measurement Unit), which accurately tracks the drone's movements and positions LIDAR points, significantly enhancing the quality and precision of the collected data [90].

Fig. 4. DJI M300 with DJI Zenmuse L1

3.2. Multispectral Sensors

Color aerial photography and infrared images have been used to monitor plant growth [91-97]. Currently, these techniques are being revisited for spatial variability analysis in fields, which is crucial for precision agriculture management because they allow for rapid image acquisition during key stages of crop development [98-107].

Unmanned Aerial Vehicles (UAVs) enable the use of lighter and more compact sensors. Drones can fly at lower altitudes than manned aircraft, which increases safety and improves the spatial resolution of the images [99-107].

In this research we used the DJI Phantom 4 Multispectral is a drone equipped with a multispectral cam-era, specifically designed for applications in precision agriculture, vegetation monitoring, and environmental research. This drone features a multispectral camera system consisting of six separate cameras, five of which capture images in different spectral bands, including Blue, Green, Red, Red Edge, and Near-Infrared, while the sixth camera is a standard RGB camera (Fig. 5). Each of the cameras has a resolution of 2 MP, allowing for the collection of detailed data in specific spectral bands, and the RGB camera additionally captures high-quality images in standard colors. The DJI Phantom 4 Multispectral is equipped with an integrated GNSS/RTK system, which provides high positioning accuracy, crucial for tasks that require precise terrain map-ping, such as crop mapping or soil studies. Additionally, the drone features a sun-light sensor mounted on top, which measures solar radiation at the time of image capture, enabling the calibration of camera data and yielding more accurate results regardless of lighting conditions. With these features, the DJI Phantom 4 Multispectral is an extremely effective tool for crop management and environmental studies [108].

Fig. 5. DJI Phantom 4 Multispectral

Drone technology has rapidly developed, and their integration with modern sensors and positioning systems (GPS and GNSS) has significantly increased since 2010 [109-111]. The availability of affordable and easy-to-use devices has made UAVs a common tool in agriculture [111-114].

Vegetation indices are important because they provide key information about the condition of vegetation, its distribution, and changes in ecosystems on a large scale. They allow for monitoring plant health, assessing crop productivity, and tracking environmental changes, which has direct applications in agriculture, natural resource management, environmental protection, and climate research [109,115,116]. In this study, the calculated indices used include NDVI, GNDVI, VARI, and MSAVI.

Normalized Difference Vegetation Index (NDVI) is a metric used to assess vegetation health based on the analysis of satellite or aerial images, including data from drones equipped with multispectral cameras. NDVI is one of the most widely used indices for monitoring plant health, crop productivity, and changes in plant ecosystems. Its operation is based on the difference between light reflected in the near-infrared range (NIR) and light reflected in the red range (RED) (Formula 3.1) [117-119].

$$NDVI = \frac{\rho^{NIR} - \rho^{RED}}{\rho^{NIR} + \rho^{RED}} \tag{3.1}$$

Healthy, actively photosynthesizing plants strongly reflect light in the near-infrared range while absorbing light in the red range. NDVI is expressed as a value ranging from -1 to +1, with high values (close to +1) indicating lush and healthy vegetation, low values (close to 0) indicating areas with sparse vegetation or plants under stress, and negative values potentially indicating the absence of vegetation or the presence of other surfaces, such as soil or water [120].

Green Normalized Difference Vegetation Index (GNDVI) is a metric used to assess vegetation health, similar to NDVI, but it utilizes light reflection in the green spectrum (Green) instead of the red spectrum (Red). GNDVI is particularly useful in precision agriculture and plant research, especially for plants more sensitive to water and nitrogen stress, which are better reflected in the green spectrum. The operation of GNDVI involves calculating the difference between light reflected in the near-infrared (NIR) range and light reflected in the green range (Green) (Formula 2) [121-123].

$$GNDVI = \frac{\rho^{NIR} - \rho^{GREEN}}{\rho^{NIR} + \rho^{GREEN}} \tag{3.2}$$

Healthy and actively photosynthesizing plants reflect light in the near-infrared range while also reflecting some light in the green range, which is measured by the GNDVI index. GNDVI values range from -1 to +1, where high values (close to +1) indicate healthy, lush vegetation, often in better condition than suggested by NDVI values, particularly in the context of water and nitrogen stress. Low GNDVI values (close to 0) indicate less healthy or stressed vegetation, while negative values usually indicate the absence of vegetation or the presence of other surfaces, such as soil or water. GNDVI has wide applications in precision agriculture, enabling better monitoring of plant health, especially in the context of water and nitrogen stress, which is crucial for crop management. This index allows for the early identification of stressed areas, which in turn enables quicker responses to issues related to water or nutrient deficiencies.

Visible Atmospherically Resistant Index (VARI) was designed to minimize the impact of atmospheric conditions on multispectral data recorded in the visible spectral range (green, red, blue) [124]. This index allows for more effective monitoring of vegetation under variable atmospheric conditions, such as fog or smoke, which can interfere with the measurements of other indices like NDVI. The Formula 3.3 for VARI is:

$$VARI = \frac{\rho^{GREEN} - \rho^{RED}}{\rho^{GREEN} + \rho^{RED} - \rho^{BLUE}} \tag{3.3}$$

This index is particularly useful in situations where atmospheric conditions may affect the quality of the data, allowing for more stable vegetation analysis across different environments.

Modified Soil Adjusted Vegetation Index (MSAVI) is a vegetation index designed to reduce the influence of soil on vegetation measurements, especially in areas with sparse vegetation where the soil is more visible. MSAVI is a modification of the standard SAVI (Soil Adjusted Vegetation Index) [125], introducing a soil adjustment factor that improves the accuracy of measurements in these challenging conditions [126]. The Formula 3.4 for MSAVI is:

$$MSAVI = \frac{2\rho NIR+1-\sqrt{(2\rho NIR+1)^2-8(\rho NIR-\rho RED)}}{2} \quad (3.4)$$

MSAVI is particularly useful for analyzing vegetation in areas with sparse coverage, where standard indices might be less accurate due to the visibility of the soil. These indices enable more precise monitoring and management of vegetation health, which is crucial in precision agriculture and environmental research.

3.3.Thermal Sensors

In recent years, similar to other applications of UAVs, there has been a significant increase in studies using thermal imagery from drones in agriculture and ecology [127]. Although the use of thermal remote sensing in forestry and ecology remains limited, initial research confirms its usefulness in areas such as fire detection [128], wildlife monitoring [129,130], assessment of water availability in ecosystems [131], and evaluation of plant growth and productivity [132]. Thermal sensors integrated with drones have great potential in applications that require precise temperature data with high spatial and temporal resolution, such as detecting tree diseases [133], assessing water stress in crops [134], and analyzing transpiration and land surface temperature changes [135].

Thermal infrared (TIR) remote sensing is considered an effective tool for collecting, analyzing, and modelling energy fluxes and temperature variations [136]. Traditional platforms, such as aircraft, satellites, or ground systems, provide valuable data on a regional scale, but their use is limited by high costs and complex operation. In comparison, small unmanned aerial systems (UAS) offer many advantages, including lower operational costs and greater accessibility [137].

The DJI Mavic 2 Enterprise Advanced (Fig.6 right) is a drone designed with professional applications in mind, including industrial inspections, search and rescue operations, infrastructure monitoring, and crisis management. One of the key features of this model is its dual-camera system, which combines a high-resolution thermal camera with an optical camera. The thermal camera, with a resolution of 640x512 pixels, enables precise detection of temperature differences with an accuracy of ±2°C, making it extremely useful for inspecting power infrastructure, buildings, and in search and rescue missions where it can assist in locating individuals in difficult conditions. The drone is also equipped with a 48 MP optical camera, capable of capturing de-tailed images and 4K video. This function is particularly valuable for documenting the technical condition of structures or creating precise 3D models. The Mavic 2 Enterprise Advanced also offers 32x digital zoom, allowing the operator to closely inspect objects from a distance, minimizing the risk of damaging the drone during flights in challenging environments. Additionally, the drone is equipped with safety systems such as obstacle avoidance sensors that operate in five directions, ensuring safe operation in complex terrain. The drone also features an RTK (Real-Time Kinematic) module, enabling precise positioning with centimeter-level accuracy, which is crucial for missions requiring high precision. The high-capacity battery provides up to 31 minutes of flight time, giving operators ample time to complete necessary tasks [138].

The DJI H20T (Fig. 6 left) is a multi-sensor thermal imaging camera designed for use with drones, specifically the DJI Matrice series. It combines a thermal camera, a high-resolution zoom camera (20MP), a wide-angle camera (12MP), and a laser rangefinder into one unit. The thermal camera offers a resolution of 640x512 pixels, ideal for detecting temperature variations in various applications like search and rescue, fire-fighting, and industrial inspections. The zoom camera supports up to 23x hybrid optical zoom and up to 200x maximum zoom, while the wide-angle camera provides a broad field of view to quickly survey large areas. The laser rangefinder measures distances up to 1,200 meters, crucial for mapping and surveying. With an IP44 rating, the H20T is built to withstand harsh environments and various weather conditions. It supports intelligent features such as AI Spot-Check and High-Res Grid Pho-to, which automate inspection tasks. The thermal camera's radiometric capabilities enable temperature measurement for every pixel, making it invaluable for detailed post-flight analysis. This payload is primarily compatible with DJI's Matrice 300 RTK, enhancing its operational capabilities across public safety, utility inspections, and environmental monitoring [139].

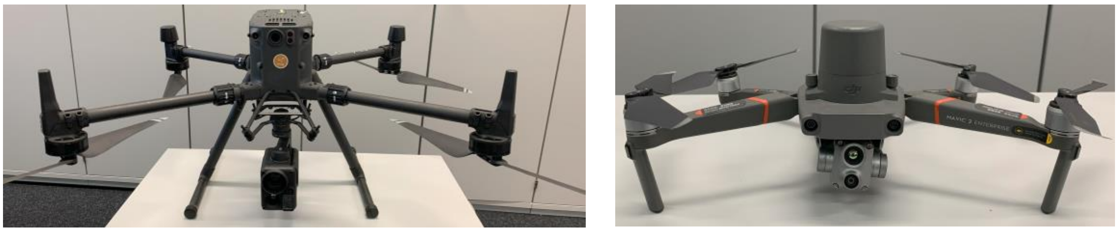

Fig. 6. DJI M300 with DJI Zenmuse H20T (left), DJI Mavic 2 Enterprise Advanced (right)

4. RESULTS

4.1. Topographic mapping with using LiDAR UAV

Figure 7 shows the terrain model with height data and point classification. The terrain is varied in elevation, as illustrated by the colour gradient from blue, indicating lower areas, to red light green, representing higher areas. The red values are giving by objects above the terrain, such as a power pole on the right. Overall, the terrain appears relatively flat, with slight slopes and local elevations, suggesting the presence of small hills or depressions. In the higher parts, there are elements visible that may correspond to natural elevations, buildings, or other structures.

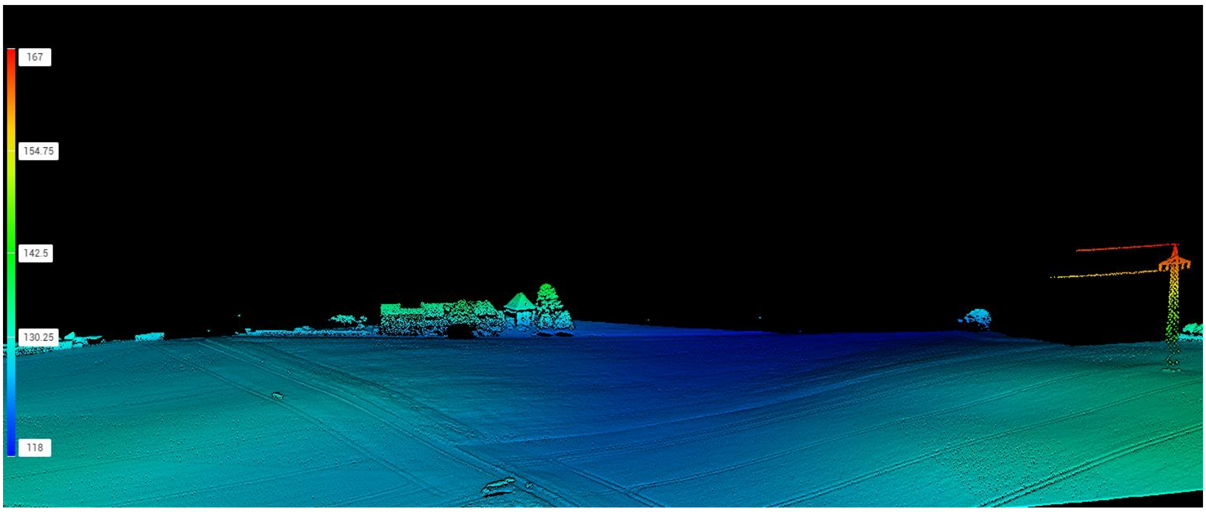

Fig. 7. Terrain model on the basis LiDAR data

Figure 8 shows the classification of points in the model, with "Ground Points" dominating, indicating a homogeneous ground surface. A few unclassified points may represent the presence of trees, shrubs, or non-standard structures. The terrain appears quite open, suggesting that it could be an agricultural area, wasteland, or recreational space.

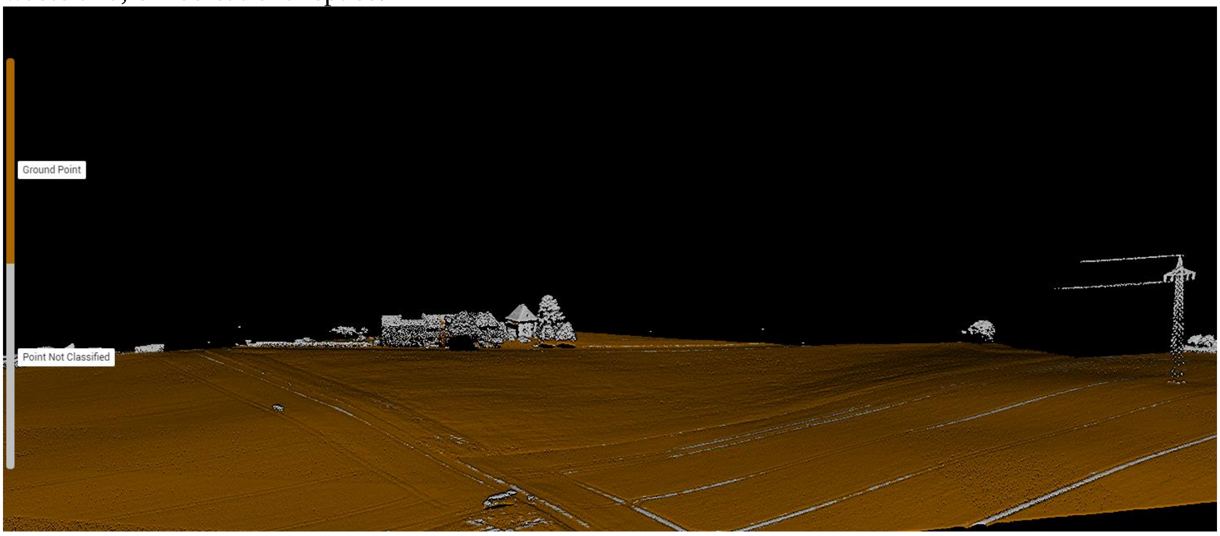

Fig. 8. Classification of the point from LiDAR data

Figure 9 presents a Digital Elevation Model (DEM), showing a height gradient from approximately 118 to 137 meters, confirming the presence of slight elevation differences. The terrain is surrounded by roads and located near built-up areas, suggesting its potential use for agricultural. The entire terrain model depicts an area with distinct but minor elevation variations, which is mostly open and sparsely built-up.

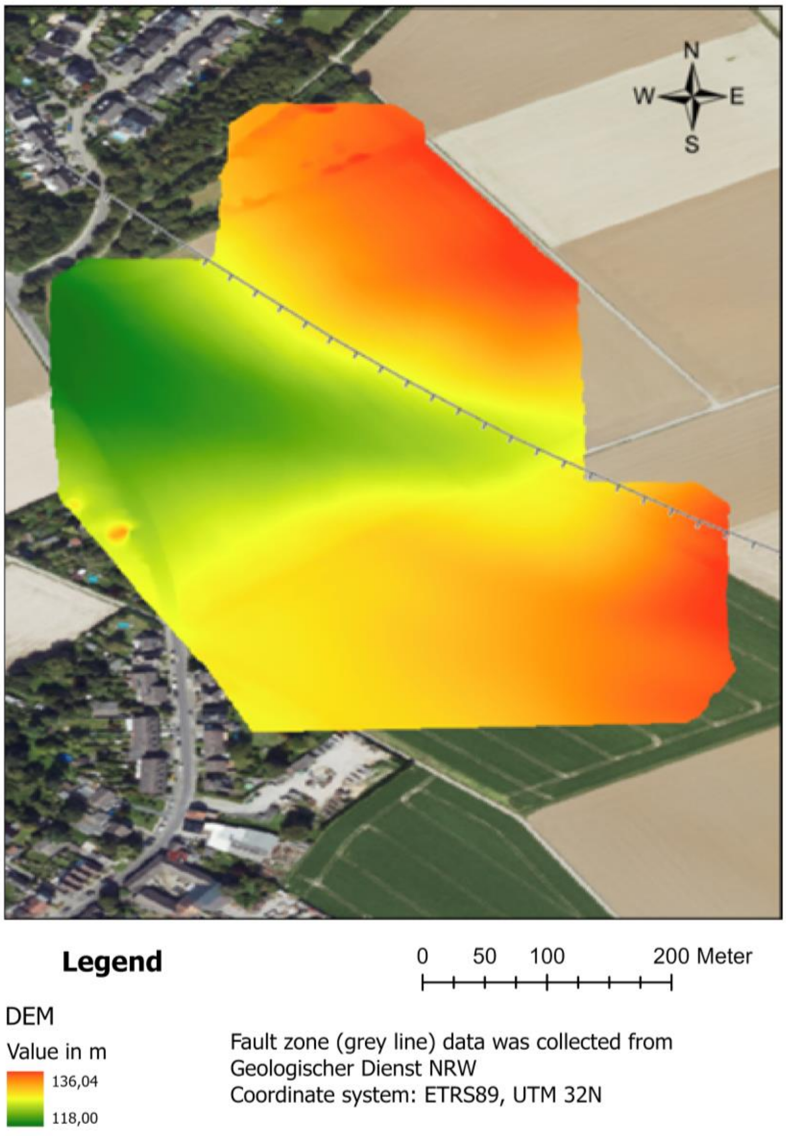

Fig. 9. Digital Elevation Model

4.2. Vegetation indices

After processing the raw images from DJI Phantom 4 Multispectral, an orthophoto was created with five channels: Red, Green, Blue, Infrared Red (IR) and Near-Infrared Red (NIR). Four vegetation indices were derived to analyze the vegetation changes in the test area, as shown in the Figure 10.

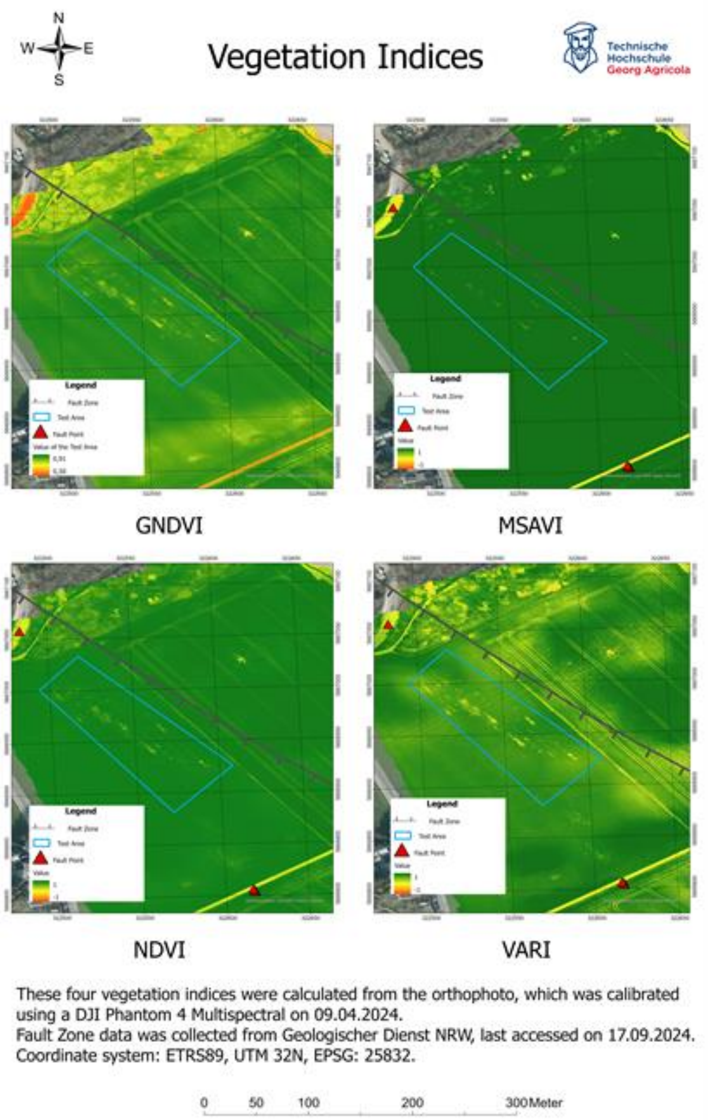

Fig. 10. Map of four vegetation indices: GNDVI (top left), MSAVI (top right), NDVI (bottom left), VARI (bottom right)

NDVI is useful to determine the density of vegetation on a patch of land. A value range of 0.3 to 0.91 indicates quite dense vegetation cover [120] and the mean is 0.89. Similarly, GNDVI with a value range of 0.15 to 0.95 and the mean 0.79 shows that the more intense the values represented by the green colour, the higher the vegetation vitality. The MSAVI index, ranging from 0.25 to 0.98 and the mean is 0.93, corresponds to the seed and leaf development stage. Lastly, the VARI – the index measures leaf coverage and estimate the fraction of vegetation in an image with low sensitivity to atmospheric effects. A higher VARI value indicates better vegetation cover, with a value range from 0 to 0.6 and the mean is 0.42 representing good quality of vegetation cover.

4.3. Thermal Orthophotomap

Thermal images were collected using the DJI Mavic 2 Enterprise Advanced and DJI Matrice 300 with DJI H20T (Fig. 11). Again, Orthophotos was created out of the raw data. In the test area marked in blue, so-called ‘hot spots’ - locations that show elevated temperature values, were observed in both calculated thermal orthophotos.

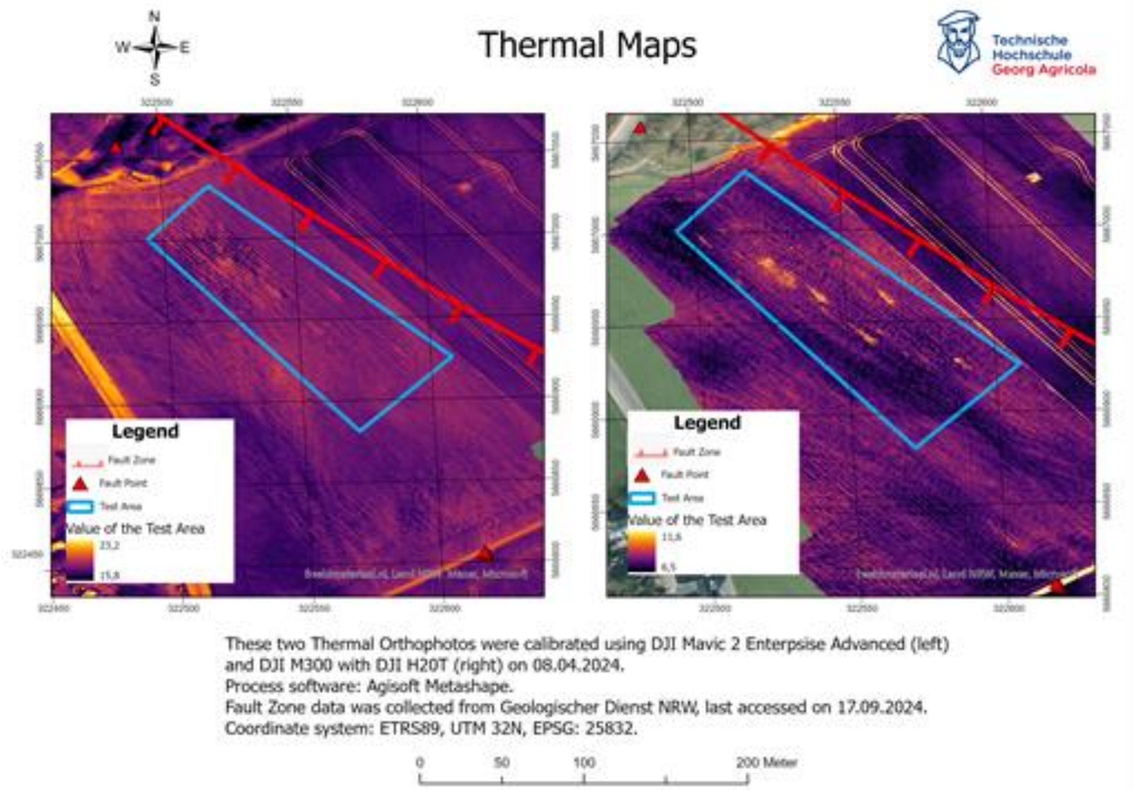

Fig. 11. Maps of thermal orthophotos from DJI Mavic 2 Enterprise Advanced (left) and DJI Matrice 300 (right)

5. DISCUSSION

The study revealed the combination between LiDAR data, multispectral images and thermal images to detect the fault zone. The LiDAR data provides highly detailed and accurate information about the study area’s surface and its features. This helps create the terrain model that presents the surface of the Earth, and DEM that present the Earth’s surface elevations so this is essential for gaining a deeper understanding of natural topography. The reason is that possibly detected structures might be a result of semi-natural processes during the agricultural work in this area. The dent or depression visible in Figures 7 to 9 together with ploughing etc. might cause soil erosion which can better be assessed using a good elevation model.

Beside vegetation indices derived from multispectral imagery are powerful tools used to assess and monitor various aspects of vegetation heath, cover and condition. By analyzing multispectral data with these vegetation indices (GNDVI, NDVI, MSAVI and VARI), the study can gain valuable insights into the health, structure and dynamics of vegetation across diverse landscapes. In this case all vegetation indices calculated and are presented in Figure 10 shows that affected areas and low developed vegetation are more or less linear and not related to the erosion processes caused by agricultural work along the depression. Last but not least, from the thermal orthophotos with temperature range reflected from the study area, temperature variations in vegetation can be shown. Healthier vegetation typically has lower temperatures due to transpiration cooling [120]. The thermal data can also complement the vegetation indices above by providing additional insights into the density and distribution of vegetation cover, specially under varying environmental conditions. In our case the results shown in Figure 11 showing the same structures as the vegetation indices, thus linear structures which are oriented in the same direction of the fault.

As shown in the Figures 10 and 11, the test area located only 39,45 meters and 43,93 meters south-west of the fault line given by geological survey maps. It exhibits vegetation changes across all four vegetation indices and thermal anomalies due to less covered soil. The generation of a line in the mapping process, which is derived from individual bore hole measurements and transferred to a map at a target scale of 1:1.500 (Vegetation Indices Map in the Figure 10), scale of 1:2.500 (Thermal Maps in the Figure 11), must always be viewed with a certain margin of error. This is completely appropriate and consistent with the results in Figure 7 and Figure 8. There is a small area located 55,35 meters (at the scale map of 1:2500) to the north-east of the fault line that also shows vegetation depressions in the Figure 10. However, from Figure 7 and Figure 8 indicated the presence of a utility pole in this area (Figure 12).

Fig. 12. The utility pole in real-life

In addition, field verification, which is shown in Figure 13, shows that there are cracks in the area of paved streets, which can be identified with the location of previously detected changes using vegetation indicators (Figure 10) and the thermal orthophotos (Figure 11).

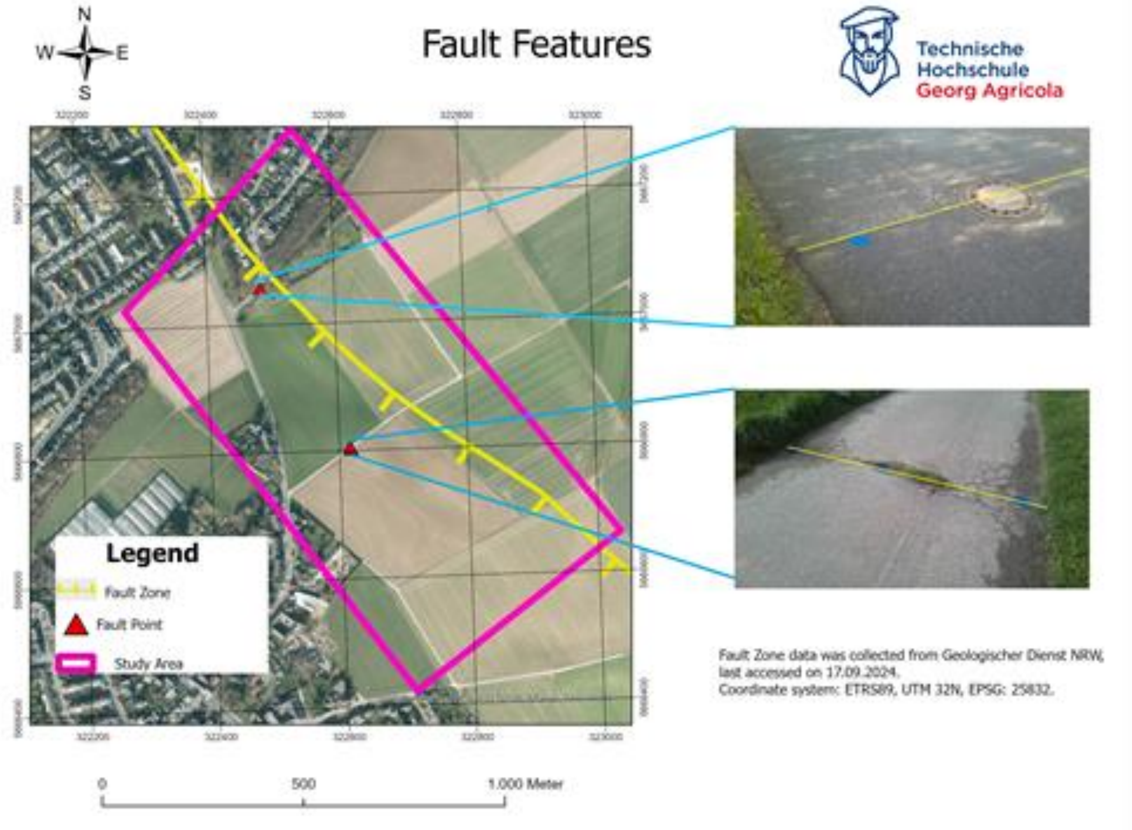

Fig. 13. Fault features with Fault Zone and Fault Points

A comparison with Moudrý et al. [140] study reveals notable methodological and conceptual differences, highlighting the broader scope and integrative nature of the approach presented in this paper. While Moudrý et al. [140] focused on evaluating the effectiveness of LiDAR and UAV imagery under "leaf-off" and "leaf-on" conditions for monitoring post-mining landscapes, our methodology is more comprehensive in both scope and application. The authors demonstrated that UAV-based structure-from-motion (SfM) data collected during the leaf-off season can produce digital terrain models (DTMs) with comparable accuracy to airborne LiDAR, particularly in forested areas. However, datasets acquired during the leaf-on season were significantly less effective because dense vegetation impeded ground surface detection, especially in areas with complex canopy structures.

In contrast, this study not only addresses these seasonal limitations, but also incorporates a synergistic combination of LiDAR, multispectral, and thermal imagery. This multimodal integration allows for a more nuanced interpretation of the terrain, enabling the detection of subsurface structural anomalies that are not apparent from elevation models alone. The addition of thermal data-absent in [140] provides valuable insight into vegetation transpiration, exposed soil surfaces, and hydrological perturbations, which serve as indirect indicators of tectonic activity and geodynamic instability

A key strength of this approach is its reduced dependency on seasonal imaging conditions. By employing thermal data and vegetation indices (e.g., NDVI, GNDVI, MSAVI, VARI), we are able to monitor surface conditions and vegetation health regardless of foliage coverage, including during full vegetation periods. This flexibility represents a major advantage over the methodology in [140], where the authors explicitly acknowledge the seasonal limitations of passive remote sensing under leaf-on conditions.

Another important distinction lies in the scale and purpose of the respective analyses. While Moudrý et al. [140] examined a larger post-mining site (61 ha) with a focus on ecological succession and restoration monitoring, our study focuses on high-resolution investigation of smaller zones to detect subtle surface deformations and identify potentially active fault structures. This higher spatial precision enables the detection of features such as surface fissures (Fig. 13), which were not addressed in [140].

Verification strategies also differ significantly. Although [140] validated their DTMs using 796 GNSS reference points, no field-based confirmation of surface deformation was performed. In our study, field verification corroborated the presence of ground fractures and deformations consistent with remote sensing anomalies, thereby enhancing the credibility of our interpretation.

In summary, our methodology advances remote sensing applications by integrating topographic, spectral, and thermal datasets, supported by ground-truth validation. Compared to [140], our approach not only overcomes seasonal limitations and increases spatial precision but also facilitates the identification of geodynamic phenomena with direct relevance to infrastructure planning, geotechnical risk management, and land use in post-mining regions. This Figure 14 displays drone data (NDVI, thermal orthophotomap, DEM) for tectonic fault detection, overlaid with a known fault line from geological survey NRW. The top layer, NDVI (green), indicates vegetation health; anomalies could suggest soil/water changes due to faulting. The middle layer, a thermal orthophotomap (purple-yellow), shows temperature variations; thermal anomalies may point to fault-related heat. The brown line from geological survey NRW represents the known Viersen fault. The bottom layer, DEM (yellow-orange-green), illustrates topography; sudden elevation changes often mark faults. The analysis aims to confirm and precisely locate the fault by comparing these drone-derived anomalies to refining geological understanding.

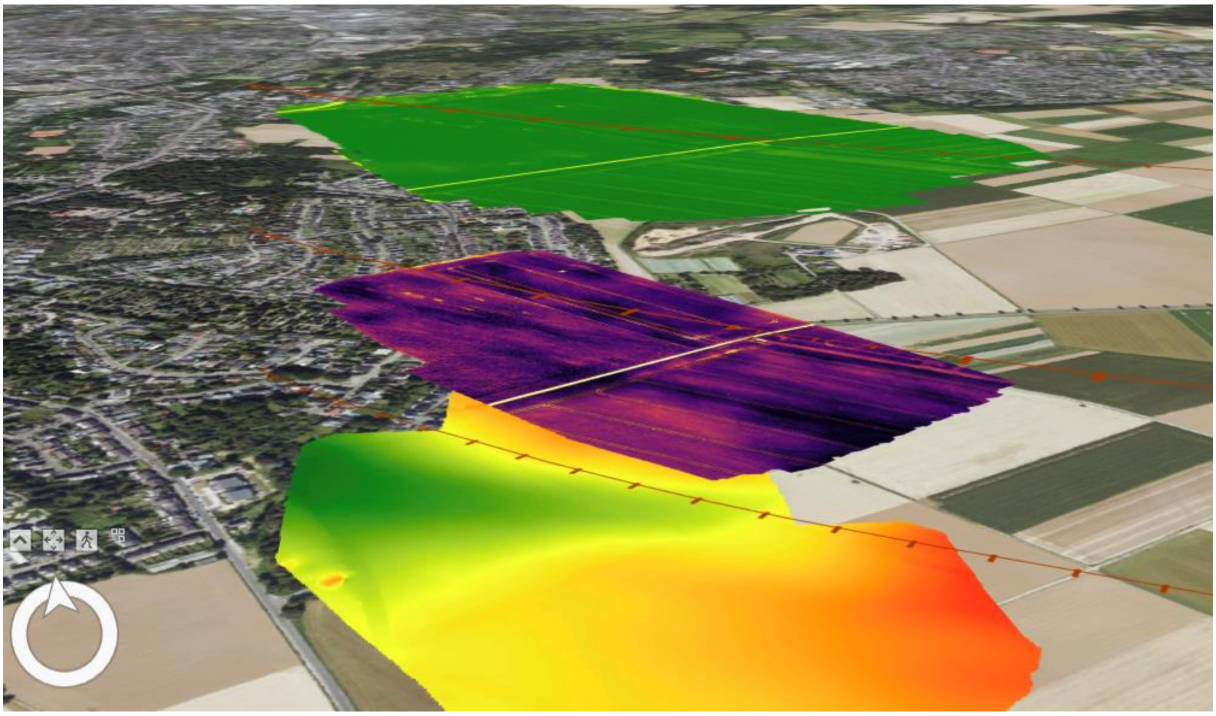

Fig. 14. Schematic presentation of: (down) Digital Elevation Model, (middle) thermal orthophotomap and (top) Normalized Difference Vegetation Index. Fault zone (brown line) data was collected from Geologischer Dienst NRW. Source of Basemaps: Digital Orthophoto from Bezirksregierung Köln

6. CONCLUSIONS

The study demonstrates that effective fault zone detection relies not merely on the quantity of data but on the complementary value provided by different sensor types. The integration of LiDAR, multispectral, and thermal data enables cross-validation of surface features that might remain ambiguous when using single-sensor analyses.

This multi-sensor approach significantly reduces dependency on seasonal and environmental conditions. For instance, thermal imaging remains effective even under dense vegetation, while vegetation indices help distinguish between natural plant stress and structurally induced anomalies. Cross-comparison across spectral, thermal, and structural domains enhances the accuracy of interpreting linear features as indicators of fault activity.

Moreover, the validation of remote sensing results with field observations bridges the gap between geospatial analysis and real-world ground conditions, increasing the practical value of the method for geotechnical risk assessment and land-use planning. Although the results are promising, future research should focus on introducing quantitative performance metrics, identifying potential sources of error or false positives, and integrating automation and machine learning to streamline data processing. The proposed methodology offers a flexible and scalable tool for geomonitoring, particularly in mining areas or tectonically active regions. Its applications include early-warning systems, infrastructure planning, and post-mining land restoration. A key conclusion is the importance of sensor diversity—limitations inherent in individual methods, such as vegetation interference in

LiDAR, atmospheric variability in thermal data, or spectral ambiguities, can be effectively mitigated through data fusion.

Compared to the study by Moudrý et al. [140], which emphasized seasonal and temporal variability in vegetation and terrain analysis, this research focuses on the synergy of data types. By incorporating thermal data alongside traditional spectral and elevation datasets, the proposed model is less sensitive to seasonal changes and therefore more suited for continuous geomonitoring—especially in areas affected by tectonic reactivation due to industrial activity, such as the Garzweiler II mine. Early fault detection in such high-risk zones can inform infrastructure planning and public safety strategies.

In conclusion, the UAV-based multi-sensor approach provides a scalable and adaptive method for monitoring dynamic landscapes. Its utility extends beyond fault detection to include slope stability monitoring, subsidence detection, and post-mining environmental assessments. Future work should prioritize the development of automated data fusion techniques, machine learning classifiers, and long-term data collection to improve model robustness and predictive capabilities.

Such advancements will support the creation of a more resilient framework for managing geohazards in both post-mining and tectonically active areas, ensuring that technology continues to aid sustainable land use and infrastructure development.

ACKNOWLEDGEMENT

The authors would thanks to company RWE to good cooperation and financed this research project.

REFERENCES

1. Shahmoradi, J et al. 2020. A Comprehensive Review of Applications of Drone Technology in the Mining Industry. *Drones*, **4(3)**, **34**,1-25.
2. Kaszowska, O 2007. Wpływ podziemnej eksploatacji górniczej na powierzchnię terenu [The impact of underground mining on the land surface]. *Problemy Ekologii* **R.11, Nr.1**, 52-57.
3. Goerke-Mallet, P, Melchers, C and Müterthies, A 2016. *Innovative monitoring measures in the phase of post-mining. Mining meets water – conflicts and solutions*. Proceedings of IMWA 2016, Leipzig, Germany, July 11-15, 570–577.
4. Directive 2011/92/EU of the European Parliament and of the Council of 13 December 2011 on the assessment of the effects of certain public and private projects on the environment https://eur-lex.europa.eu/legal-content/EN/TXT/?uri=CELEX%3A32011L0092 (last accessed 15 October 2024).
5. Johansen, K et al. 2019. Using Unmanned Aerial Vehicles to assess the rehabilitation performance of open cut coal mines. *Journal of Cleaner Production*, **209,1**, 819-833.
6. Kim, D-P et al. 2022. Analysis of Mine Change Using 3D Spatial Information Based on Drone Image. *Sustainability*, **14(6)**, **3433**, 1-15.
7. Pawlik, M et al. 2022. Analyse des Zustands der Vegetation auf dem Gelände des stillgelegten Bergwerks Prosper Haniel anhand von multispektralen Satellitenbildern der Sentinel-2 Mission und Drohnenflüge [Analysis of the vegetation condition on the site of the closed Prosper Haniel mine using multispectral satellite images from the Sentinel-2 mission and drone flights]. *Markscheidewesen* **129**, 37–44.
8. Ludovisi, R et al. 2017. UAV-based thermal imaging for high-throughput field phenotyping of black poplar response to drought. *Frontiers in Plant Science* **8, 1681,** 1-18.

9. Manfreda, S et al. 2018. On the Use of Unmanned Aerial Systems for Environmental Monitoring. *Remote Sens*ing **10, 641**, 1-28.
10. Bernsdorf, B et al. 2023. Multisensorales Geomonitoring—Ein Beitrag zur Datenfusion im Nachbergbau = Multi-Sensoral Geomonitoring—A Contribution on Data Fusion in Post-Mining. *gis.Science* **1**, 1–16.
11. Booysen, R, Gloaguen, R, Lorenz, S, Zimmermann, R and Nex, PA 2020. Geological Remote Sensing. In Alderton, D and Scott A. Elias, SA (eds) *Reference Module in Earth Systems and Environmental Sciences, 2nd Edition*. Amsterdam: Elsevier. Volume 64, 267–274.
12. Jackisch, R et al. 2018. Drone-borne hyperspectral monitoring of acid mine drainage: An example from the Sokolov lignite district. *Remote Sens*ing **10 (3), 385**, 1-23.
13. Flores, H et al. 2021 Uas-based hyperspectral environmental monitoring of acid mine drainage affected waters. *Minerals* **11 (2), 182,** 1-25.
14. Flores, H, Reker, B, Pawlik, M, Haske, B and Rudolph, T 2024. *Hyperspectral UAV-sensing for monitoring tailing ponds: Towards responsible resource repurposing*. Proceedings of the 15th International Mine Water Association Conference & West Virginia Mine Drainage Task Force Symposium, Morgantown, WV, USA. April 21–26, 193-195.
15. Erdelj, M and Natalizio, E 2016. *UAV-assisted disaster management: Applications and open issues.* Proceedings of 2016 International Conference on Computing, Networking and Communications (ICNC 2016), Kauai, HI, USA, February 15–18, 1-5.
16. Xu, J, Ota, K and Dong, M 2019. *LUNA: Lightweight UAV navigation based on airborne vision for disaster management.* Proceedings of International Conference on Internet of Things (iThings) and IEEE Green Computing and Communications (GreenCom) and IEEE Cyber, Physical and Social Computing (CPSCom) and IEEE Smart Data (SmartData), Atlanta, GA, USA, July 14–17, 315-322.
17. Bouguettaya, A et al. 2022. A review on early wildfire detection from unmanned aerial vehicles using deep learning-based computer vision algorithms. *Signal Processing* **190, 108309**, 1-14.
18. Yuan, G et al. 2021. Accuracy assessment and scale effect investigation of UAV thermography for underground coal fire surface temperature monitoring. *International Journal of Applied Earth Observation and Geoinformation* **102, 102426**, 248-254.
19. Prosekov, AY et al. 2022. Environmental monitoring of endogenous fires based on thermal imaging and 3D mapping from an unmanned aerial vehicle. *IOP Conference Series Earth and Environmental Science* **981, 4201**, 1-7.
20. Bernsdorf, B et al. 2020. Possibilities of a method for copter-supported gas leak detection with thermal imaging cameras in industry and hazard prevention. *Oil Gas European Magazine* **4**, 12–20.
21. Mader, S et al. 2021. Sicherheit von gastechnischen Anlagen—Das KaMonSys-Projekt. Teil 2: Bildverarbeitungsansätze für eine mehrstufige Gasdetektion mittels Satelliten- und Kopter-Lösungen [Safety of gas technology systems—The KaMonSys Project. Part 2: Image processing approaches for multi-level gas detection using satellite and drone solutions]. *Erdöl-Erdgas-Kohle* **137 (6)**, 23–29.
22. Rudolph, T et al. 2021. Das Projekt KaMonSys–Sicherheit in gastechnischen Anlagen: Teil 1: Grundlagen—3D-GIS und Flugplanung für autonome Roboterflüge in gastechnischen Anlagen [The KaMonSys Project – Safety in Gas Technology Systems: Part 1: Fundamentals – 3D GIS and Flight Planning for Autonomous Robot Flights in Gas Technology Systems]. *Erdöl-Erdgas-Kohle* 137 (5), 26–33.
23. Haske, B et al. 2022. Sustainability in Energy Storage—How Modern Geoscience Concepts can Improve Underground Storage Monitoring. *International Journal of Earth and Environmental Sc*iences **7, 199**, 1-9.

24. Haske, B et al. 2023. The use of UAVs in supporting the preservation of the industrial and mining heritage in the Ruhr area. *IOP Conference Series: Earth and Environmental Science* **1189, 12024**, 1-18.
25. Sondaj, L and Górecka-Żwirska, A 2015. Monitoring zagrożeń naturalnych w PGE GIEK S.A. Oddział KWB Turów [Monitoring of natural hazards at PGE GIEK S.A. Turów Lignite Mine Division]. *Górnictwo Odkrywkowe* **56, 4**, 28-32.
26. Langhammer, J 2019. UAV Monitoring of Stream Restorations. *Hydrology* **6 (2), 29**,1-22.
27. Niethammer, U et al. 2012. UAV-based remote sensing of the Super-Sauze landslide: Evaluation and results. *Engineering Geology* **128**, 2-11.
28. Carvajal, F, Agüera, F and Pérez, M 2011. *Surveying a landslide in a road embankment using Unmanned Aerial Vehicle photogrammetry*. International Archives of the Photogrammetry, Remote Sensing and Spatial Information Sciences, Vol. XXXVIII-1/C22 UAV-g 2011, Conference on Unmanned Aerial Vehicle in Geomatics, Zurich, Switzerland, 1–6.
29. Rau, JY, Jhan, JP, Lo, CF and Lin, YS 2011. *Land slide mapping using imagery acquired by a fixed-wing UAV*. International Archives of the Photogrammetry, Remote Sensing and Spatial Information Sciences, Vol. XXXVIII-1/C22, ISPRS Zurich 2011 Workshop, Zurich, Switzerland, September 14-16, 195–200.
30. Lucieer, A et al. 2014. Mapping Landslide Displacements using Structure from Motion (SfM) and Image Correlation of Multi-temporal UAV Photography. *Progress in Physical Geography* **38 (1)**, 97-116.
31. Turner, D et al. 2015. Time Series Analysis of Landslide Dynamics Using an Unmanned Aerial Vehicle (UAV). *Remote Sensing* **7 (2)**, 1736-1757.
32. Torrero, L, Seoli, L, Molino, A, Giordan, D, Manconi, A, Allasia, P and Baldo, M 2014. The Use of Micro-UAV to Monitor Active Landslide Scenarios. In: Lollino, G, Manconi, A, Guzzetti, F, Culshaw, M, Bobrowsky, P and Luino, F (eds) *Engineering Geology for Society and Territory - Volume 5*. Springer, Cham, 701-704.
33. El Mohtar, CS, Abou-Jaoude, G, Abdullah, C and Harb, J 2016. The Kfarnabrakh Landslide of November 30th, 2015: A Geological and Geotechnical Evaluation of the Landslide and Risk of Future Failures. GEER Association Report No. GEER-047.2015.
34. Greenwood, W, Zekkos, D, Clark, MK, Lynch, JP, Bateman, J and Chamlagain, D 2016. *UAV-Based 3-D Characterization of Rock Masses and Rock Slides in Nepal*. Proceedings of 50th US Rock Mechanics/Geomechanics Symposium, Houston, Texas, June 26-29, 1-4.
35. Jovančevič, SD et al. 2016. Analysis of a historical landslide in the Rjecina River Valley, Croatia. *Geoenvironmental Disasters* **3, 26**, 1-9.
36. Zekkos, D, Manousakis, J, Greenwood, W and Lynch, J 2016. *Immediate UAV-enabled Infrastructure Reconnaissance following Recent Natural Disasters: Case Histories from Greece*. Proceedings of 1st International Conference on Natural Hazards & Infrastructure, Chania, Greece, June 28-30, 1-9.
37. Casagli, N et al. 2017. Space borne, UAV and ground-based remote sensing techniques for landslide mapping, monitoring and early warning, *Geoenvironmental Disasters* 4,9, 1–23.
38. Zekkos, D, Manousakis, J, Athanasopoulos-Zekkos, A, Clark, M, Knoper, L, Massey, C, Archibald, G, Greenwood, W, Hemphill-Haley, M, Rathje, E, Litchfield, N, Medwedeff, W, Van Dissen, RJ, Kearse, J, Ries, W, Villamor, P and Langridge, RM 2018. *Structure-from-Motion based 3D mapping of landslides & fault rupture sites during 2016 Kaikoura earthquake reconnaissance.* Proceedings of 11th U.S. National Conference on Earthquake Engineering, Integrating Science, Engineering & Policy, Los Angeles, California, June 25-29,1-10.

39. Bednarczyk, Z 2019. Zagrożenia osuwiskowe w polskich odkrywkowych kopalniach węgla brunatnego, przykłady przeciwdziałania oraz możliwości zastosowania zdalnego monitoringu w celu ograniczenia ryzyka [Landslide hazards in Polish open-pit lignite mines, examples of countermeasures, and the potential use of remote monitoring to reduce risk]. *Biuletyn Państwowego Instytutu Geologicznego* **477**, 1–20.
40. Tannant, DD 2015. Review of Photogrammetry-Based Techniques for Characterization and Hazard Assessment of Rock Faces. *International Journal of Geohazards and Environment* **1(2)**, 76–87.
41. Tannant, DD et al. 2017. Characterization and analysis of a translational rockslide on a stepped-planar slip surface. *Engineering Geology* **220**, 144–151.
42. Török, Á et al. 2018. Slope stability and rockfall assessment of volcanic tuffs using RPAS with 2D FEM slope modelling. *Natural Hazards and Earth System Sciences* **18**, 583–597.
43. Saroglou, C, Kallimogiannis, V, Bar, N, Manousakis, G and Zekkos, D 2019. *Analysis of slope instabilities in the Corinth Canal using UAV-enabled mapping*. Proceedings of the ICONHIC 2nd International Conference on Natural Hazards & Infrastructure, Chania, Greece, June 23–26, 1-8.
44. Gao, M et al. 2017. High-resolution mapping based on an Unmanned Aerial Vehicle (UAV) to capture paleoseismic offsets along the Altyn-Tagh fault. *China Scientific Reports* **7, 8281**, 1-11.
45. Menegoni, N et al. 2018. Analysis by UAV Digital Photogrammetry of Folds and Related Fractures in the Monte Antola Flysch Formation (Ponte Organasco, Italy). *Geosciences* **8 (8), 299**, 1-16.
46. Török, Á et al. 2020. Application of UAV in Topographic Modelling and Structural Geological Mapping of Quarries and Their Surroundings-Delineation of Fault-Bordered Raw Material Reserves. *Sensors* **20 (2), 489**, 1-19.
47. Tibaldi, A et al. 2021. Mapping and evaluating kinematics and the stress and strain field at active faults and fissures: a comparison between field and drone data at the NE rift, Mt Etna (Italy), *Solid Earth* **12**, 801–816.
48. Soil Map of NRW 1:50000 – Geological Survey of North-Rhein Westfalia, Data License – Germany – attribution - version 2.0, WMS Service: https://www.wms.nrw.de/gd/bk050? (last accessed 15 October 2024).
49. Klostermann, J 1992. Das Quartär der Niederrheinischen Bucht: Ablagerungen der letzten Eiszeit am Niederrhein [The Quaternary of the Lower Rhine Basin: Deposits from the last Ice Age in the Lower Rhine region]. Krefeld: Geologisches Landesamt Nordrhein-Westfalen.
50. Ahorner, L 1962. Untersuchungen zur quartären Bruchtektonik der Niederrheinischen Bucht [Studies on Quaternary Fault Tectonics of the Lower Rhine Basin]. *E&G Quaternary Science Journal* **13**, 24–105.
51. Zagwijn, WH and Hager, H 1987. Correlations of continental and marine Neogene deposits in the south-eastern Netherlands and the Lower Rhine District. *Mededelingen van de Werkgroep voor Tertiaire en Kwartaire Geologie* **24 (1-2)**, 59-78.
52. Schäfer, A et al. 1996. Cyclic sedimentation in Tertiary Low-er-Rhine Basin (Germany)—the ‘Liegendrücken’ of the brown-coal open-cast Fortuna mine. *Sedimentary Geology* **103 (3-4),** 229-247.
53. Lücke, A et al. 1999. Environmental history of the German Lower Rhine Embayment during the Middle Miocene as reflected by carbon isotopes in brown coal. *Palaeogeography, Palaeoclimatology, Palaeoecology* **154(4)**, 339-352.
54. Klett, M et al. 2002. Facies interpretation from well logs applied to the Tertiary Lower Rhine Basin fill. *Netherlands Journal of Geosciences / Geologie en Mijnbouw* **81(2)**, 167-176.
55. Camelbeeck, T, Vanneste, K, Alexandre, P, Verbeeck, K, Petermans, T, Rosset, P, Everaerts, M, Warnant, R, and Van Camp, M 2007. Relevance of active faulting and seismicity studies to assessments of long-term earthquake activity and maximum magnitude in intraplate northwest

Europe, between the Lower Rhine Embayment and the North Sea. In: Stein, S and Mazzotti S (eds) *Continental Intraplate Earthquakes: Science, Hazard, and Policy Issues*, Geological Society of America, 193-224.

56. Reicherter, K, Froitzheim, N and Jarosinski, M 2008. Alpine tectonics north of the alps. In: McCann, T (ed) *The geology of central europe mesozoic and cenozoic.* London: The Geological Society of London, 1-52.
57. Gerwin, W et al. 2023. Perspectives of lignite post-mining landscapes under changing environmental conditions: what can we learn from a comparison between the Rhenish and Lusatian region in Germany? *Environmental Science Europe* **35, 36**, 1-24.
58. Prinz, L et al. 2018. The geometry, distribution and development of sand bodies in the Miocene-age Frimmersdorf Seam (Garzweiler open-cast mine), Lower Rhine Basin, Germany: implications for seam exploitation. *Geological Magazine* **155 (3)**, 685-706.
59. Walter, R 2007. Geologie von Mitteleuropa 7., vollständing neu bearbeitete Auflage [Geology of Central Europe, 7th Edition, Completely Revised]. Stuttgart: Schweizerbart.
60. Ahorner, L 1983. Historical seismicity and present-day activity of the Rhenish Massif, central Europe. In: Fuchs, K., von Gehlen, K, Mälzer, H, Murawski, H and Semmel, A (eds.), *Plateau Uplift, the Rhenish Shield—A Case History*, Berlin, Springer-Verlag, 198–221.
61. Ahorner, L 1985. The general pattern of seismotectonic dislocations in central Europe as the background for the Liège earthquake on November 8, 1983. In: Melchior, P (ed) *Seismic activity in Western Europe*, Dordrecht: Springer, 41–56.
62. Pilz, M, Nievas, C, Cotton, F, Prehn, K, Razafindrakoto, H, Schorlemmer, D, Weatherill, G, Spies, T and Lege, T 2020. *Seismic risk analysis in Germany: an example from the Lower Rhine Embayment. Final report, (Scientific Technical Report STR; 20/02)*, Potsdam: GFZ German Research Centre for Geosciences.
63. Hinzen, KG et al. 2021. Seismicity in the Northern Rhine Area (1995–2018). *Journal of Seismology* **25**, 351–367.
64. Gold, RD et al. 2017. Apparent late Quaternary fault-slip rate increase in the southern Lower Rhine graben, Central Europe. *Bulletin of the Seismological Society of America* **107(2)**, 563-580.
65. Grützner, C et al. 2016. Holocene surface ruptures of the Rurrand Fault, Germany—insights from palaeoseismology, remote sensing and shallow geophysics. *Geophysical Journal International* **Volume 204, Issue 3**, 1662–1677.
66. Hinzen, KG et al. 2004. On the resolution of H/V measurements to determine sediment thickness, a case study across a normal fault in the Lower Rhine Embayment, Germany. *Journal of Earthquake Engineering* **8(06)**, 909-926.
67. Pilz, M et al. 2021. Regional broad-band ground-shaking modelling over extended and thick sedimentary basins: an example from the Lower Rhine Embayment (Germany). *Bulletin of Earthquake Engineering* **19**, 581–603
68. Görres, B and Kuhlmann, H 2007. How groundwater withdrawal and recent tectonics cause damages of the earth's surface: Monitoring of 3D site motions by GPS and terrestrial measurements. *Journal of Applied Geodesy* **1(4)**, 223-232.
69. Petri, R 2015. *Securing Final and Border Slopes in the Open-Pit Lignite Mines of the Rhenish Mining District from the Perspective of the Mining Authority*. In: Niemann-Delius, C (ed) Proceedings of the 12th International Symposium Continuous Surface Mining, Aachen, 567-576.
70. LuftVG -Luftverkehrsgesetz https://www.gesetze-im-internet.de/luftvg/BJNR006810922.html (last accessed 15 October 2024).
71. LuftVO (Luftverkehrs-Ordnung) https://www.gesetze-im-internet.de/luftvo_2015/BJNR189410015.html (last accessed 15 October 2024).

72. LuftVZO (Luftverkehrs-Zulassungs-Ordnung https://www.gesetze-im-internet.de/luftvzo/BJNR003700964.html (last accessed 15 October 2024).
73. Commission Implementing Regulation (EU) 2019/947 of 24 May 2019 on the rules and procedures for the operation of unmanned aircraft https://eur-lex.europa.eu/legal-content/EN/TXT/?uri=CELEX%3A32019R0947 (last accessed 15 October 2024).
74. Lin, Y-C et al. 2019. Evaluation of UAV LiDAR for Mapping Coastal Environments. *Remote Sensing* **11 (24), 2893**, 1-32.
75. Estornell, J et al. 2012. Assessment of factors affecting shrub volume estimations using airborne discrete-return LIDAR data in Mediterranean areas. *Journal of Applied Remote Sensing* **6(1), 063541**,1-10.
76. Weligepolage, K et al. 2012. Surface roughness analysis of a conifer forest canopy with airborne and terrestrial laser scanning techniques. *International Journal of Applied Earth Observation and Geoinformation* **14**, 192–203.
77. Montreuil, AL et al. 2013. Decadal and seasonal development of embryo dunes on an accreting macrotidal beach: North Lincolnshire, *UK. Earth Surface Processes and Landforms* **38**, 1851–1868.
78. Bater, CW and Coops, NC 2009. Evaluating error associated with lidar-derived DEM interpolation. *Computers and Geosciences* **35(2)**, 289–300.
79. Hancock, GR 2006. The impact of different gridding methods on catchment geomorphology and soil erosion over long timescales using a landscape evolution model. *Earth Surface Processes and Landforms* **31(8)**, 1035–1050.
80. Moloney, JG et al. 2017. Coastal Dune Surveying Using a Low-Cost Remotely Piloted Aerial System (RPAS). *Journal of Coastal Research,* **34**, 1244–1255.
81. Westoby, MJ et al. 2018. Cost-effective erosion monitoring of coastal cliffs. *Coastal Engineering* **138**, 152–164.
82. Mancini, F et al. 2013. Using unmanned aerial vehicles (UAV) for high-resolution reconstruction of topography: The structure from motion approach on coastal environments. *Remote Sensing* **5 (12)**, 6880–6898.
83. Sankey, TT et al. 2010. Characterizing western juniper expansion via a fusion of Landsat 5 thematic mapper and lidar data. *Rangeland Ecology and Management* **63 (5)**, 514–523.
84. Houser, C et al. 2008. Controls on coastal dune morphology, shoreline erosion and barrier island response to extreme storms. *Geomorphology* **100 (3-4)**, 223-240.
85. Turner, D et al. 2012. An automated technique for generating georectified mosaics from ultra-high resolution unmanned aerial vehicle (UAV) imagery, based on structure from motion (SfM) point clouds. *Remote Sensing* **4 (5)**, 1392–1410.
86. Wallace, L et al. 2012. Development of a UAV-LiDAR system with application to forest inventory. *Remote Sensing* **4 (6)**, 1519–1543.
87. Miura, N, Yokota, S, Koyanagi, TF and Yamada, S 2018. *Herbaceous Vegetation Height Map on Riverdike Derived from UAV LiDAR Data*. IGARSS 2018–2018 IEEE International Geoscience and Remote Sensing Symposium, Valencia, Spain, 22–27 July, 5469–5472.
88. Zhu, X et al. 2019. Integrating UAV optical imagery and LiDAR data for assessing the spatial relationship between mangrove and inundation across a subtropical estuarine wetland. *ISPRS Journal of Photogrammetry and Remote Sensing* **149**, 146–156.
89. Pu, S et al. 2019. Real-time powerline corridor inspection by edge computing of UAV Lidar data. *International Archives of the Photogrammetry, Remote Sensing and Spatial Information Sciences* **4213**, 547–551.
90. DJI Zenmuse L1 https://www.dji.com/de/support/product/zenmuse-l1 (last accessed 15 October 2024).

91. Colewell, RN 1956. Determining the prevalence of certain cereal crop diseases by means of aerial photography. *Hilgardia* **26 (5)**, 223–286.
92. Blackmer, TM et al. 1996. Analysis of aerial photography for nitrogen stress within corn fields. *Agronomy Journal* **88 (5)**, 729–733.
93. GopalaPillai, S and Tian, L 1999. In-field variability detection and spatial yield modeling for corn using digital aerial imaging. *Transactions of the ASAE* **42 (6)**, 1911–1920.
94. Yang, C et al. 2000. Mapping grain sorghum growth and yield variations using airborne multispectral digital imagery. *Transactions of the ASAE* **43 (6)**, 1927–1938.
95. Flowers, M et al. 2003. Quantitative approaches for using color infrared photography for assessing in-season nitrogen status in winter wheat. *Agronomy Journal* **95 (5)**, 1189–1200.
96. Sripada, RP et al. 2007. Aerial color infrared photography to optimize in-season nitrogen fertilizer recommendations in winter wheat. *Agronomy Journal* **99 (6)**, 1424–1435.
97. Hunt, ER Jr et al. 2010. Acquisition of NIR-Green-Blue digital photographs from unmanned aircraft for crop monitoring. *Remote Sensing* **2 (1)**, 290–305.
98. Hunt, ER Jr., Daughtry, CST, Walthall, CL, McMurtrey, JE III and Dulaney, WP 2003. *Agricultural remote sensing using radio-controlled model aircraft*. In VanToai, T, Major, D, McDonald, M, Schepers, J and Tarpley, L (eds) Digital Imaging and Spectral Techniques: Applications to Precision Agriculture and Crop Physiology, Volume 66. Madison, WI, USA: ASA, CSSA and SSSA ,191–199.
99. Fouché, PS 1999. Detecting nitrogen deficiency on irrigated cash crops using remote sensing methods. *South African Journal of Plant and Soil* **16:2**, 59–63.
100. Fouché, PS and Booysen, NW 1994. Assessment of crop stress conditions using low altitude aerial color-infrared photography and computer image processing. *Geocarto International* **9**(**2)**, 25–31.
101. Quilter, MC and Anderson, VJ 2001. A proposed method for determining shrub utilization using (LA/LS) imagery. *Journal of Range Managemt* **54 (4)**, 378–381
102. Herwitz, SR et al. 2004. Imaging from an unmanned aerial vehicle: agricultural surveillance and decision support. *Computers and Electronics in Agriculture* **44 (1)**, 49–61.
103. Hunt, ER Jr et al. 2005. Evaluation of digital photography from model aircraft for remote sensing of crop biomass and nitrogen status. *Precision Agriculture* **6**, 359–378.
104. Jensen, T et al. 2007. Detecting the attributes of a wheat crop using digital imagery acquired from a low-altitude platform. *Computers and Electronics in Agriculture* **59 (1-2)**, 66–77.
105. Swain, KC et al. 2007. Suitability of low-altitude remote sensing for estimating nitrogen treatment variations in rice cropping for precision agriculture adoption. *Journal of Applied Remote Sensing* **1 (1), 013547**.
106. Lelong, CCD et al. 2008. Assessment of unmanned aerial vehicles imagery for quantitative monitoring of wheat crop in small plots. *Sensors* **8 (5)**, 3557–3585.
107. Berni, JAJ et al. 2009. Thermal and narrowband multispectral remote sensing for vegetation monitoring from an un-manned aerial vehicle. *IEEE Transactions on Geoscience and Remote Sensing* **47 (3)**, 722–738.
108. DJI Phantom 4 Multispectral https://www.dji.com/de/p4-multispectral/specs (last accessed 15 October 2024).
109. Tardaguila, J et al. 2021. Smart applications and digital technologies in viticulture: A review. *Smart Agricultural Technology* **1, 100005**, 1-13.
110. Aasen, H et al. 2018. Quantitative remote sensing at ultra-high resolution with UAV spectroscopy: A review of sensor technology, measurement procedures, and data correction workflows. *Remote Sens.* **10 (7), 1091**, 1-42.

111. Di Gennaro, SF et al. 2022. Spectral Comparison of UAV-Based Hyper and Multispectral Cameras for Precision Viticulture. *Remote Sensing* **14(3), 449**, 1-21.
112. Matese, A and Di Gennaro, SF 2015. Technology in precision viticulture: A state of the art review. *International Journal of Wine Research* **7**, 69–81.
113. Ammoniaci, M et al. 2021. State of the Art of Monitoring Technologies and Data Processing for Precision Viticulture. *Agriculture* **11 (3), 201**, 1-20.
114. Assmann, JJ et al. 2018. Vegetation monitoring using multispectral sensors—Best practices and lessons learned from high latitudes. *Journal of Unmanned Vehicle Systems* **7 (1)**, 54–75.
115. Giovos, R et al. 2021. Remote Sensing Vegetation Indices in Viticulture: A Critical Review. *Agriculture* **11 (5), 457**, 1-20.
116. Matese, A, Berton, A, Di Gennaro, S.F, Gatti, M, Squeri, C and Poni, S 2021. *Testing performance of UAV-based hyperspectral imagery in viticulture*. In: Stafford, JV (ed) Precision Agriculture '21. Wageningen Academic Publishers: Wageningen, The Netherlands; Budapest, Hungary, 509–516.
117. Rouse, JW, Haas, RH, Deering, DW and Schell, JA 1973. *Monitoring the Vernal Advancement and Retrogradation (Green Wave Effect) of Natural Vegetation*. Remote Sensing Center. Texas University, 1-87.
118. Tucker, CJ 1979. Red and photographic infrared linear combinations for monitoring vegetation. *Remote Sensing of Environment* **8(2)**, 127-150.
119. Huete, AR et al. 2002. Overview of the radiometric and biophysical performance of the MODIS vegetation indices. *Remote Sensing of Environment* **83 (1-2)**, 195-213.
120. Kuechly, H, Cozacu, A, Kodl, G, Nicolai, C and Vallentin, C 2020. *Grundlagen der Fernerkundung, (Inforeihe SAPIENS: Satellitendaten für Planung, Industrie, Energiewirtschaft und Naturschutz) [Fundamentals of Remote Sensing, (SAPIENS:Satellite data for planning, industry, energy management and nature conservation]*. Potsdam: Deutsches GeoForschungsZentrum GFZ.
121. Gitelson, AA and Merzlyak, MN 1998. Remote sensing of chlorophyll concentration in higher plant leaves. *Advances in Space Research* **22(5)**, 689-692.
122. Gitelson, AA et al. 1996. Use of a green channel in remote sensing of global vegetation from EOS-MODIS. *Remote Sensing of Environment* **58 (3)**, 289-298.
123. Haboudane, D et al. 2004. Hyperspectral vegetation indices and novel algorithms for predicting green LAI of crop canopies: Modeling and validation in the context of precision agriculture. *Remote Sensing of Environment* **90 (3)**, 337-352.
124. Gitelson, AA et al. 2002. Novel algorithms for remote estimation of vegetation fraction. *Remote Sensing of Environment* **80 (1)**, 76-87.
125. Huete, AR 1988. A soil-adjusted vegetation index (SAVI). *Remote Sensing of Environment* **25 (3)**, 295-309.
126. Qi, J et al. 1994. A modified soil adjusted vegetation index. *Remote Sensing of Environment* **48 (2)**, 119-126.
127. Maes, WH et al. 2017. Optimizing the Processing of UAV-Based Thermal Imagery. *Remote Sensing* **9 (5), 476,** 1-17.
128. Christensen, BR 2015. Use of UAV or remotely piloted aircraft and forward-looking infrared in forest, rural and wildland fire management: Evaluation using simple economic analysis. *New Zealand Journal of Forestry Sciences.* **45, 16**. 1-9.
129. Gonzalez, LF et al. 2016. Unmanned Aerial Vehicles (UAVs) and Artificial Intelligence Revolutionizing Wildlife Monitoring and Conservation. *Sensors* **16 (1), 97**, 1-18.
130. Chretien, LP et al. 2016. Visible and thermal infrared remote sensing for the detection of white-tailed deer using an unmanned aerial system. *Wildlife Society Bulletin* **40 (1)**, 181–191.

131. Gonzalez-Dugo, V et al. 2013. Using high resolution UAV thermal imagery to assess the variability in the water status of five fruit tree species within a commercial orchard. *Precision Agriculture* **14**, 660–678.
132. Dillen, M et al. 2016. Productivity, stand dynamics and the selection effect in a mixed willow clone short rotation coppice plantation. *Biomass and Bioenergy* **87**, 46–54.
133. Calderón, R et al. 2013. High-resolution airborne hyperspectral and thermal imagery for early detection of Verticillium wilt of olive using fluorescence, temperature and narrow-band spectral indices. *Remote Sensing of Environment* **139**, 231–245
134. Zarco-Tejada, PJ et al. 2012. Fluorescence, temperature and narrow-band indices acquired from a UAV platform for water stress detection using a micro-hyperspectral imager and a thermal camera. *Remote Sensing of Environment* **117**, 322–337.
135. Brenner, C et al. 2018. Estimation of evapotranspiration of temperate grassland based on high-resolution thermal and visible range imagery from unmanned aerial systems. *International Journal of Remote Sensing* **39 (15-16)**, 5141–5174.
136. Virtue, J et al. 2021. Thermal Sensor Calibration for Unmanned Aerial Systems Using an External Heated Shutter. *Drones* **5 (4), 119**, 1-15.
137. Sheng, H, Chao, H, Coopmans, C, Han, J, McKee, M, and Chen, Y 2010. *Low-cost UAV-based thermal infrared remote sensing: Platform, calibration and applications*. 2010 IEEE/ASME International Conference on Mechatronic and Embedded Systems and Applications, QingDao, China, 38-43.
138. DJI Mavic 2 Enterprise Advance https://enterprise.dji.com/de/mavic-2-enterprise-advanced/specs (last accessed 15 October 2024).
139. DJI H20T https://enterprise.dji.com/de/zenmuse-h20-series/specs (last accessed 15 October 2024).
140. Moudrý,V et al. 2019. Comparison of leaf-off and leaf-on combined UAV imagery and airborne LiDAR for assessment of a post-mining site terrain and vegetation structure: Prospects for monitoring hazards and restoration success. *Applied Geography* **104,** 32-41.